

## Bootstrapped Dimensional Crossover of a Spin Density Wave

Anjana M. Samarakoon,<sup>1</sup> J. Strempler<sup>2</sup>,<sup>3</sup> Junjie Zhang,<sup>1,3</sup> Feng Ye<sup>4</sup>, Yiming Qiu,<sup>5</sup> J.-W. Kim,<sup>2</sup> H. Zheng,<sup>1</sup> S. Rosenkranz<sup>1</sup>, M. R. Norman<sup>1</sup>, J. F. Mitchell<sup>1</sup> and D. Phelan<sup>1</sup>


<sup>1</sup>Materials Science Division, Argonne National Laboratory, Lemont, Illinois 60439, USA

<sup>2</sup>Advanced Photon Source, Argonne National Laboratory, Lemont, Illinois 60439, USA

<sup>3</sup>State Key Laboratory of Crystal Materials, Shandong University, 250100 Jinan, Shandong, China

<sup>4</sup>Neutron Scattering Division, Oak Ridge National Laboratory, Oak Ridge, Tennessee 37830, USA

<sup>5</sup>NIST Center for Neutron Research, National Institute of Standards and Technology, Gaithersburg, Maryland 20899, USA

 (Received 16 August 2022; revised 1 September 2023; accepted 8 September 2023; published 27 October 2023)

Quantum materials display rich and myriad types of magnetic, electronic, and structural ordering, often with these ordering modes either competing with one another or “intertwining,” that is, reinforcing one another. Low-dimensional quantum materials influenced strongly by competing interactions and/or geometric frustration are particularly susceptible to such ordering phenomena and thus offer fertile ground for understanding the consequent emergent collective quantum phenomena. Such is the case of the quasi-2D materials  $R_4\text{Ni}_3\text{O}_{10}$  ( $R = \text{La}, \text{Pr}$ ), in which intertwined charge- and spin-density waves (CDW and SDW) on the Ni sublattice have been identified and characterized. Not unexpectedly, these density waves are largely quasi-2D as a result of weak coupling between planes, compounded with magnetic frustration. In the case of  $R = \text{Pr}$ , however, we show here that exchange coupling between the transition-metal and rare-earth sublattices upon cooling overcomes both obstacles, leading to a dimensional crossover into a fully 3D-ordered and coupled SDW state on both sublattices, as an induced moment on notionally nonmagnetic  $\text{Pr}^{3+}$  opens exchange pathways in the third dimension. In the process, the structure of the SDW on the Ni sublattice is irreversibly altered, an effect that survives reheating of the material until the underlying CDW melts. This “bootstrapping” mechanism linking incommensurate SDWs on the two sublattices illustrates a new member of the multitude of quantum states that low-dimensional magnets can express, driven by coupled orders and modulated by frustrated exchange pathways.

DOI: [10.1103/PhysRevX.13.041018](https://doi.org/10.1103/PhysRevX.13.041018)

Subject Areas: Condensed Matter Physics, Magnetism, Strongly Correlated Materials

### I. INTRODUCTION

Exchange interactions between  $3d$  and  $4f$  moments play an important role in quantum materials phenomenology, exemplified by multiferroicity in  $\text{TbMnO}_3$  [1] and topological transport phenomena (anomalous Hall effect) in the geometrically frustrated pyrochlore  $\text{Nd}_2\text{Mo}_2\text{O}_7$  [2]. Because of the spatial extent of the relevant wave functions, the  $3d$ - $3d$  coupling is typically stronger than the  $3d$ - $4f$  interactions. Thus, a preordered transition-metal sublattice, in turn, may impart its magnetic structure onto the rare-earth sublattice, which orders either on its own for rare earths with magnetic ground states or via exchange coupling in singlet systems with low-lying magnetic excited states. These kinds of “imprintings” of the  $3d$

order onto the  $4f$  sublattice are not uncommon phenomena. Examples include layered nickelates and cuprates, viz.,  $\text{Pr}_2\text{NiO}_4$  [3] and  $\text{Nd}_2\text{CuO}_4$  [4]. Far less common, an ordered  $4f$  moment can leave its mark on the ordered  $3d$  system. Of the few examples of this effect,  $\text{DyVO}_3$  stands out, in which the Dy-V interaction leads to a change of orbital order in the V-O subsystem [5–7]. Also reported is an interfacial spin reorientation effect in a  $\text{LaNiO}_3$ - $\text{ScDyO}_3$  heterostructure [8].

Here, we present a manifestation of reciprocal  $3d$  to  $4f$  and  $4f$  to  $3d$  exchange coupling in the layered transition-metal oxide  $\text{Pr}_4\text{Ni}_3\text{O}_{10}$  (PNO). PNO exhibits a quasi-2D incommensurate spin density wave (SDW) on the  $3d$  Ni sublattice, established at a metal-to-metal transition  $T_{\text{MMT}} \approx 158$  K, that then transforms into a long-range-ordered 3D structure of stacked SDWs at  $T_f \approx 26$  K. At this temperature, a singular form of magnetic dimensional crossover occurs through a “bootstrapping” mechanism, whereby the SDW of the quasi-2D-ordered transition-metal sublattice induces a counterpart SDW on the rare-earth sublattice, which would otherwise be nonmagnetic due to the singlet

---

Published by the American Physical Society under the terms of the [Creative Commons Attribution 4.0 International license](https://creativecommons.org/licenses/by/4.0/). Further distribution of this work must maintain attribution to the author(s) and the published article's title, journal citation, and DOI.

crystal-field ground state of the non-Kramers  $\text{Pr}^{3+}$  ion in a low-symmetry site. In turn, the induced order of the second sublattice opens a new magnetic exchange pathway perpendicular to the layers, allowing it to bootstrap the 3D-ordered state of both rare-earth and transition-metal sublattices. The resulting interlayer correlations expressed through a reconstructed transition-metal SDW in which the Ni spins rotate by  $90^\circ$  and the magnetic  $c$  axis repeat distance doubles, become frozen in as a metastable, long-range-ordered spin modulation. Upon reheating, even well above the rare-earth ordering temperature  $T_f$ , these metastable correlations survive on the Ni sublattice, albeit with a greatly reduced 3D correlation length, until they are finally erased by the melting of the intertwined density wave state at  $T_{\text{MMT}}$ . We propose a model spin Hamiltonian to quantitatively explain these phenomena, including the evolution of magnetic states, the thermal hysteresis, and the observed quasi-2D to 3D crossover.

The crystal structure of  $R_4\text{Ni}_3\text{O}_{10}$  ( $R = \text{Pr}, \text{La}$ ) is formed by nickel-oxide trilayer slabs ( $R_2\text{Ni}_3\text{O}_8$ ) separated by rare-earth oxide bilayer slabs ( $R_2\text{O}_2$ ). As shown in Fig. 1(a), the two sublattices are interleaved by a lattice-centering translation, in which Ni trilayers and  $R$  bilayers alternate [see Fig. 1(b) and Supplemental Material Fig. S13, Ref. [9]]. As discussed in Ref. [10], the space group of  $R_4\text{Ni}_3\text{O}_{10}$  is monoclinic,  $P2_1/a$ . However, the deviation from orthorhombic space group  $Bmab$  is small, and we use this symmetry herein. The  $B$  centering of the lattice leads to an in-plane translation of  $(1/2, 0)$  between successive Ni trilayer blocks along  $c$ . Thus, within a Ni trilayer, the Ni layers are in registry (since they are separated by one  $R_2\text{O}_2$  layer), but subsequent trilayers are out of registry (since they are separated by two  $R_2\text{O}_2$  layers). This atomic arrangement is expected to favor quasi-2D antiferromagnetic order within the trilayer blocks yet simultaneously hinder a truly long-range-ordered 3D magnetic state of the

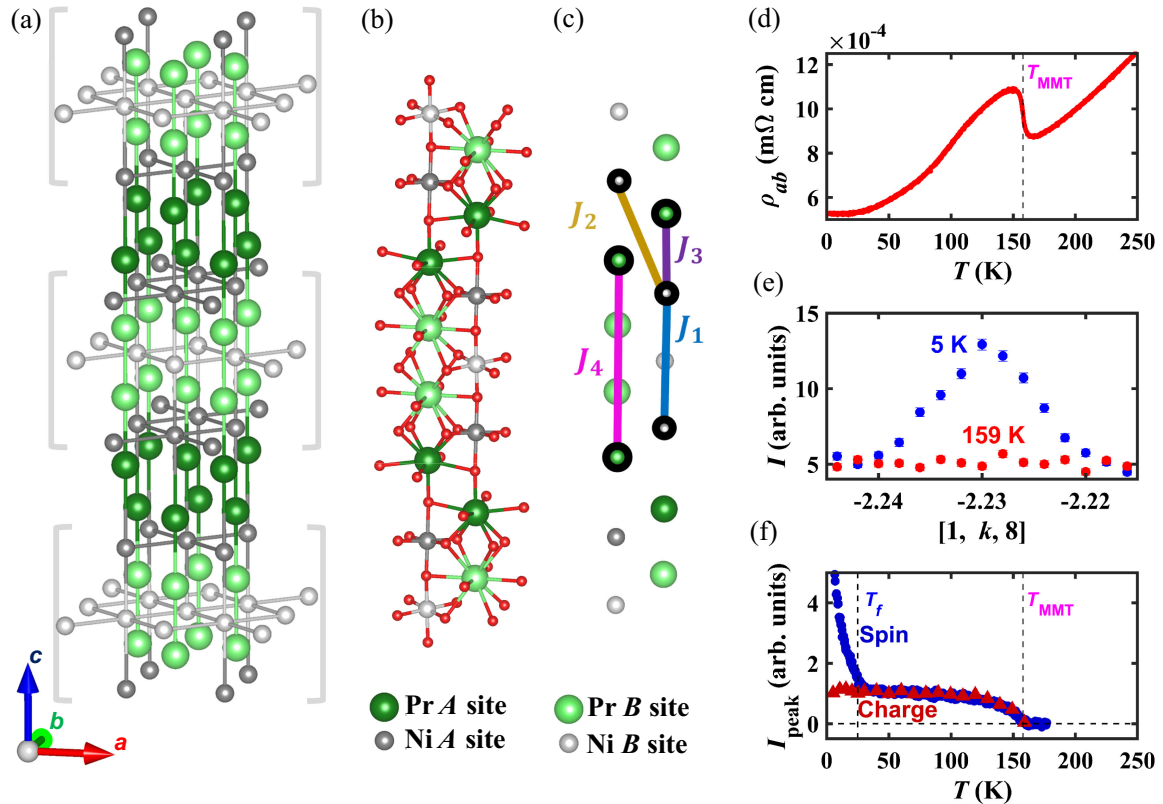


FIG. 1. (a) Crystal structure of  $R_4\text{Ni}_3\text{O}_{10}$  ( $R = \text{La}, \text{Pr}$ ) with oxygen ions omitted for clarity. The brackets indicate the nickel trilayers. (b) Part of the nuclear unit cell with corresponding O ligands. (c) Same structure as (b) but with the oxygen ligands and bonds removed. Exchange interactions are marked as single-color solid lines with open-circle ends, and the color scheme matches the labels of the exchanges ( $J_x, x = 1, 2, 3, 4$ ). Here,  $J_1$  and  $J_2$  couple Ni A sites,  $J_3$  couples Ni A sites with Pr A sites, and  $J_4$  couples Pr A sites. (d) In-plane resistivity ( $\rho_{ab}$ ) of  $\text{Pr}_4\text{Ni}_3\text{O}_{10}$  [10]. (e) CDW peak measured with x rays along  $[1, k, 8]$  at 5 K and the background at 159 K. (f) Normalized temperature dependence of the CDW peak measured by x rays at  $Q = (1, -2.23, 8)$  (red triangles) and the SDW peak at  $Q = (0, -0.6, -4.6)$ , which lies close to one of the maxima in the low-temperature phase (blue circles). Note that the breadth of the peak and limited wave-vector resolution along  $c^*$  allows for the capture of the order parameter despite a 0.1-r.l.u. offset from the peak center. The x-ray data in (e) and (f) are collected with 6.439-keV photons.

Ni-3*d* electrons because of (i) a substantial spatial separation along the *c* axis through the  $R_2O_2$  block and (ii) a geometric frustration akin to that found in  $K_2NiF_4$  [11] that hinders the development of a unique 3D ground state for antiferromagnetic interactions of ordered moments between neighboring trilayers.

Both  $La_4Ni_3O_{10}$  and  $Pr_4Ni_3O_{10}$  undergo metal-metal transitions that are manifest as anomalies in electrical transport data at  $T_{MMT}$  [12,13], which is approximately 148 K for  $La_4Ni_3O_{10}$  and 158 K for  $Pr_4Ni_3O_{10}$  [10], as shown in Fig. 1(d). Recent single-crystal x-ray- and neutron-diffraction work on  $La_4Ni_3O_{10}$  established that incommensurate magnetic and structural peaks appear at  $T_{MMT}$  upon cooling [14]. Augmented by band-structure calculations, these observations were interpreted as a coupled CDW and antiferromagnetic SDW with twice the charge wavelength in a Fermi-surface-nesting-driven picture. Importantly, all charge and spin ordering in  $La_4Ni_3O_{10}$  is thought to occur within the trilayer perovskite units, and specifically, the CDW and SDW are centered on nickel sites based on structure factor calculations [14]. A model was proposed in which the SDWs with opposite polarization occur on the upper and lower layers within a Ni trilayer with the middle Ni layer being nonmagnetic. The core electrons of  $La^{3+}$  cations are uninvolved in the CDW, and given that it is nonmagnetic, the role of  $La^{3+}$  is entirely steric.  $Pr^{3+}$  cations, on the other hand, have partially filled *f*-shells ( $4f^2$ ), which makes magnetic ordering possible for this sublattice, though this also requires an appreciable exchange field to overcome its symmetry-governed crystal-field singlet ground state (this is discussed in detail in the Supplemental Material Sec. VI, Ref. [9]). It also opens the potential for intersublattice  $3d$ - $4f$  exchange interactions in  $Pr_4Ni_3O_{10}$ . Indeed, here we show that such exchange pathways provide a mechanism for overcoming both roadblocks to 3D order discussed above—intertrilayer separation and geometric frustration—leading to the novel bootstrapping and imprinting behavior expressed by this intertwined density wave system.

## II. RESULTS

### A. Experiments

Consistent with the convention of Ref. [14], in diffraction experiments we refer to a face-centered unit cell of dimensions approximately equal to  $5.4 \times 5.4 \times 27 \text{ \AA}^3$ , such that the CDW wave vector is along  $\mathbf{b}$ , which is at a  $45^\circ$  angle to the Ni—O bonds in the basal plane [see Fig. 1(a)]. This setting is a  $\sqrt{2} \times \sqrt{2} \times 1$  supercell of a body-centered tetragonal setting of approximately  $3.9 \times 3.9 \times 27 \text{ \AA}^3$ . Unpolarized x-ray-diffraction measurements, sensitive to charge, are taken through the anticipated CDW wave vector (see Ref. [14]), and a peak is observed only below  $T_{MMT}$  as shown in Fig. 1(e) at  $Q = (1, -2.23, 8)$ , with an order parameter labeled as “charge” in Fig. 1(f). This charge-order

parameter turns on at  $T_{MMT}$ . Measurements of a CDW peak performed as a function of the x-ray energy near the Ni *K* edge show a shift in the energy at which the CDW peak is observed compared to the fluorescence [see Fig. 2(a)]. This shift is a hallmark of a contribution from the anomalous Ni scattering and is thus indicative of a significant contribution of the nickel electrons to the CDW. Thus, in concert with our previous band-structure calculations and structure factor arguments [14], we confirm that the CDW in  $Pr_4Ni_3O_{10}$  originates from Ni-3*d* electrons. We note that the CDW order parameter [Fig. 1(f)] shows no anomalies below  $T_{MMT}$ ; rather, the temperature dependence is consistent with a single transition at  $T_{MMT}$ . We conclude from these observations that  $La_4Ni_3O_{10}$  and  $Pr_4Ni_3O_{10}$  behave alike in the charge sector.

Neutron-diffraction experiments were performed on both  $Pr_4Ni_3O_{10}$  and  $La_4Ni_3O_{10}$  to assess their magnetic order (for details, see Sec. VI). Figures 3(a) and 3(b) show the neutron-diffraction intensities collected in the  $(0kl)$  scattering plane for both  $Pr_4Ni_3O_{10}$  (left panels) and  $La_4Ni_3O_{10}$  (right panels) at 6 and 50 K. The CDW peaks at the wave vectors anticipated from the x-ray experiments are apparently too weak to be observed due to the significantly lower flux in the neutron experiments compared to the synchrotron x rays, and the temperature-dependent superlattice peaks with  $\mathbf{q}_{SDW} \approx (0, 0.6, 0)$  are magnetic. Note that corresponding measurements at  $T = 200 \text{ K}$  ( $>T_{MMT}$ ) are treated as a nonmagnetic background and subtracted from the rest of the data. At 50 K, which is below  $T_{MMT}$  for both samples, similar cigar-shaped magnetic peaks are observed at  $k \approx 0.6$  and  $1.4$  and  $l \approx 2$  and  $6$ . Incommensurability in *k* can be understood as an in-plane SDW coupled to the CDW, obeying the relation  $2\mathbf{q}_{SDW} = \mathbf{q}_{CDW}$  [14]. The readily apparent anisotropic nature of the magnetic peaks clearly indicates that the magnetic order is quasi-2D within the basal plane. However, as shown in Figs. 3(c) and 3(d), the *l* dependence of each incommensurate peak is complex. As we discuss below, extensive modeling of short-ranged order among multiple-layer stacking patterns is required to describe this scattering intensity, including both  $Q$  dependences and peak widths. In contrast, CDW peaks as shown in Fig. 2(b) are significantly narrower, indicative of longer-range correlations along *c* in the charge sector.

The neutron-diffraction pattern for  $La_4Ni_3O_{10}$  remains unchanged at 6 K compared to 50 K, as it contains only a single magnetic phase transition at  $T_{MMT}$  due to the Ni-3*d* electrons. In contrast, a quite different pattern is observed at 6 K for  $Pr_4Ni_3O_{10}$ . The magnetic peaks appear at the same incommensurate values of *k* as at 50 K, but the *l* dependence, intensities, and shapes of the peaks are all dramatically modified. The peaks now appear sharp at  $l = n/2$  (where *n* is odd), which indicates that the magnetic unit cell has doubled along *c*. As we show below, this reflects an irreversible alteration of the SDW on the Ni sublattice as well as an ordering of Pr moments. The

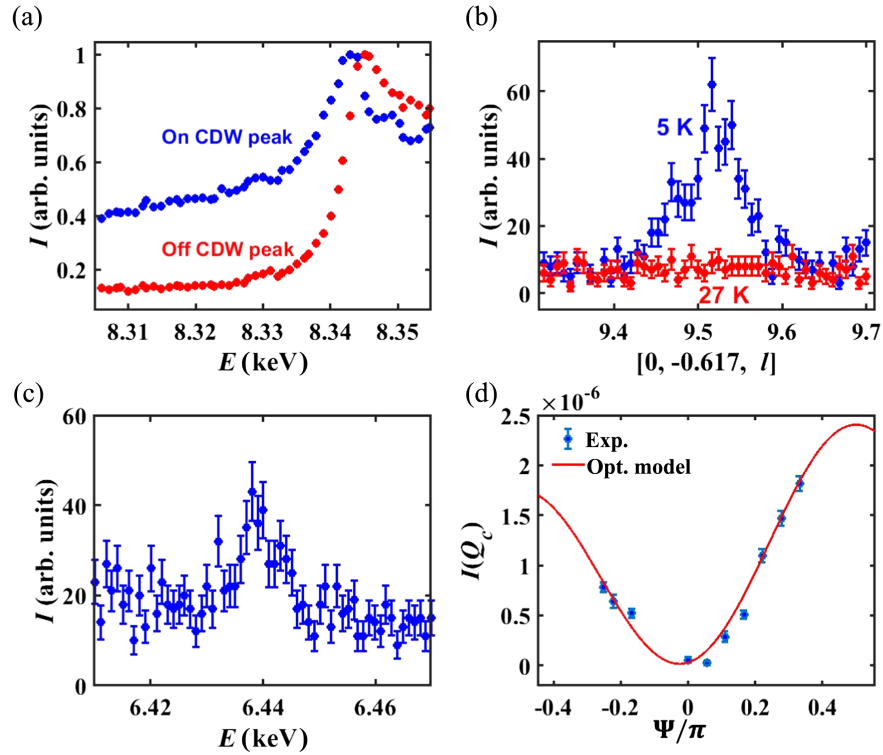


FIG. 2. Resonant x-ray scattering. (a) Energy scans around the Ni K edge on and off the CDW Bragg peak showing the energy dependence of the CDW peak and the fluorescence background, respectively. (b) The polarized resonant peak at  $\mathbf{Q} = (0, -0.617, 9.5)$  showing the Pr magnetic moment ordering at 5 K but not at 27 K. (c) Energy dependence of the peak showing resonance at the Pr  $L_2$  edge. (d) The resonant peak integrated intensity as a function of the azimuthal angle  $\Psi$  in comparison to (solid red line) that calculated from the optimized model with Pr moments along  $\mathbf{b}$ . The resonant peak itself as a function of  $\Psi$  is shown in Supplemental Material Fig. S7(a), Ref. [9]. Note that all error bars in this and other figures represent 1 standard deviation. The x-ray data in (b) and (d) are collected with 6.439-keV photons.

breadth of the peaks along  $l$  drastically diminishes [see Fig. 3(c)], reflecting a crossover to 3D magnetic order [see inset of Fig. 3(c)]. The redistribution of intensity combined with the absence of such phenomena in  $\text{La}_4\text{Ni}_3\text{O}_{10}$  suggests that the Pr-4*f* electrons are responsible for driving the system from quasi-2D order to 3D order. The order parameter associated with the two magnetic transitions can be tracked by the temperature-dependent intensity at fixed  $\mathbf{Q} = (0, -0.6, -4.6)$ , which overlaps with the magnetic intensities in both the lower- $T$  and higher- $T$   $\text{Pr}_4\text{Ni}_3\text{O}_{10}$  phases and is displayed as the “spin” order parameter in Fig. 1(f). The gradual change with the temperature below  $T_f \approx 26$  K, indicative of the second ordering, is suggestive of an induced moment ordering, presumably on Pr, rather than a conventional phase transition [15–19].

To confirm this Pr-specific moment ordering, resonant polarized x-ray-scattering experiments were performed around the Pr  $L_2$  edge (see Sec. VI B). Figure 2(b) shows scans through  $\mathbf{Q}_{\text{RXS}} = (0, -0.617, 9.5)$ . Scattering in the  $\sigma\text{-}\pi'$  polarization channel renders this configuration sensitive only to magnetic order, and the resonance makes the sensitivity specific to Pr. Indeed, a

temperature-dependent peak visible at 5 K but not at 27 K confirms the ordering of Pr-4*f* moments in the ground-state phase, as the x-ray energy dependence of the peak shown in Fig. 2(c) is consistent with resonance at the Pr  $L_2$  edge. Furthermore, we observe a gradual increase in the strength of this peak below 27 K [see Supplemental Material Fig. S7(b), Ref. [9]], and the temperature trend again is consistent with an induced moment transition. Finally, we observe an azimuthal ( $\Psi$ ) dependence of the resonant scattering that is consistent with magnetic dipolar order of the Pr ions with an intensity governed by the formula  $I \propto \boldsymbol{\varepsilon}_{\text{in}} \times \boldsymbol{\varepsilon}_{\text{out}} \cdot \mathbf{M}$ , where  $\boldsymbol{\varepsilon}_{\text{in}}$ ,  $\boldsymbol{\varepsilon}_{\text{out}}$ , and  $\mathbf{M}$  represent the polarizations of the incoming and outgoing x rays and the magnetic dipolar moment of the Pr ions, respectively. As shown in Fig. 2(d), the data follow this formula (given by the solid red curve), and the direction of the Pr moment is approximately along  $\mathbf{b}$  (the best fit yields an approximately  $8^\circ$  cant out of the basal plane) at 5 K (more information can be found in Supplemental Material Sec. II, Ref. [9]).

An examination of the  $T$ -dependent neutron-diffraction intensity along  $l$  allows us to understand qualitatively the relationship of the spin order between the low- $T$  state ( $T < T_f$ ), the intermediate- $T$  state ( $T_f < T < T_{\text{MMT}}$ ),



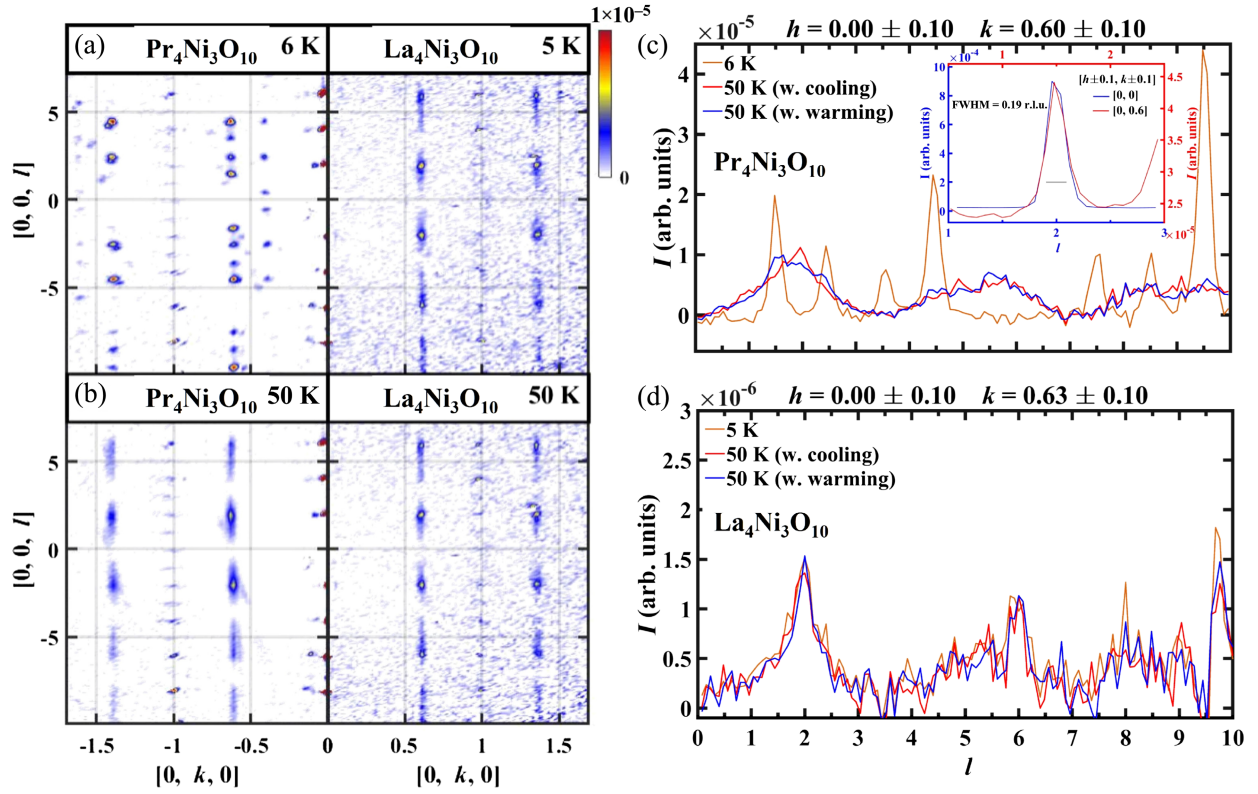


FIG. 3. Neutron-scattering data collected on CORELLI. Slices along  $[0kl]$  for (left)  $\text{Pr}_4\text{Ni}_3\text{O}_{10}$  and (right)  $\text{La}_4\text{Ni}_3\text{O}_{10}$ . Samples measured at (a) approximately 6 K and (b) 50 K after cooling directly from the paramagnetic phase. Panels (c) and (d) show the line cuts along  $l$  at  $h = 0 \pm 0.1$  and  $k = 0.6 \pm 0.1$  for  $\text{Pr}_4\text{Ni}_3\text{O}_{10}$  and  $\text{La}_4\text{Ni}_3\text{O}_{10}$ , respectively. Data are collected at 50 K twice while cooling to and warming from base temperature (approximately 6 K). The data measured at 200 K ( $>T_{\text{MMT}}$ ) are treated as a nonmagnetic background and subtracted (see Supplemental Material Sec. I, Ref. [9]). Inset: The nuclear Bragg peaks along  $l$  at  $h = 0 \pm 0.1$  and  $k = 0 \pm 0.1$  for  $\text{Pr}_4\text{Ni}_3\text{O}_{10}$  are compared to the line cut through the SDW. The similar line shape indicates a lack of distinguishable finite-size broadening along  $c$  within the constraint of the wave-vector resolution of the measurement on CORELLI. The in-plane correlation length of the SDW below  $T_{\text{MMT}}$  is also comparable to that of the CDW and the nuclear structure.

and the high- $T$  state ( $T > T_{\text{MMT}}$ ) of  $\text{Pr}_4\text{Ni}_3\text{O}_{10}$  (see Supplemental Material Sec. I, Ref. [9]). As shown in Figs. 4(a) and 4(c), the line shapes in the intermediate temperature state differ markedly on cooling versus warming. Specifically, a comparison of the diffuse signal in this intermediate-temperature state reveals a clear spectral weight distribution biased toward  $l \approx (n/2)$  ( $n$  odd) during warming from the low- $T$  state. Thus, the  $c$ -axis ordering of the SDW established in the low- $T$  structure with ordered Pr moments imprints itself onto the Ni magnetic sublattice on warming, even in the absence of rare-earth magnetic order. For  $T_f < T < T_{\text{MMT}}$ , the imprinting manifests as a short-range order that is absent on cooling. This kind of metastable imprinting on the SDW configuration, and the concomitant hysteresis in the scattering pattern, is presumably driven by the Ni-3d to Pr-4f exchange coupling. Noting that this hysteretic imprinting on the Ni-centered SDW and the accompanying modification of its magnetic structure have not been observed previously to our knowledge, we now provide quantitative models that justify these claims.

### III. MODELING AND DATA FITTING

We explored a variety of numerical models accompanied by an iterative optimization procedure (IOP) to fit the experimentally measured neutron-scattering intensities,  $I^{\text{exp}}(\mathbf{Q})$  (see Sec. VI E) for the ordered state in  $\text{La}_4\text{Ni}_3\text{O}_{10}$ , as well as the three proposed ordered states of  $\text{Pr}_4\text{Ni}_3\text{O}_{10}$ : the ground state (LowT), the intermediate-temperature state on warming (IntW), and the intermediate-temperature state on cooling (IntC).

We begin by considering the case of  $\text{La}_4\text{Ni}_3\text{O}_{10}$ , which exhibits only a single, quasi-2D magnetic phase. Based on limited data collected with a triple-axis spectrometer along  $l$ , we previously proposed [14] that each individual Ni trilayer consists of a simple sinusoidal SDW in the top and bottom layers of equal magnitude with a  $\pi$  phase difference between the two layers; the middle layer has no ordered moment in this picture. As we allude to above, next-neighboring trilayers are structurally equivalent under a translational symmetry operation of  $[1/2, 0, 1/2]$  (equivalent to a body-centering translation in the tetragonal setting), and the proposed SDW phase is invariant under

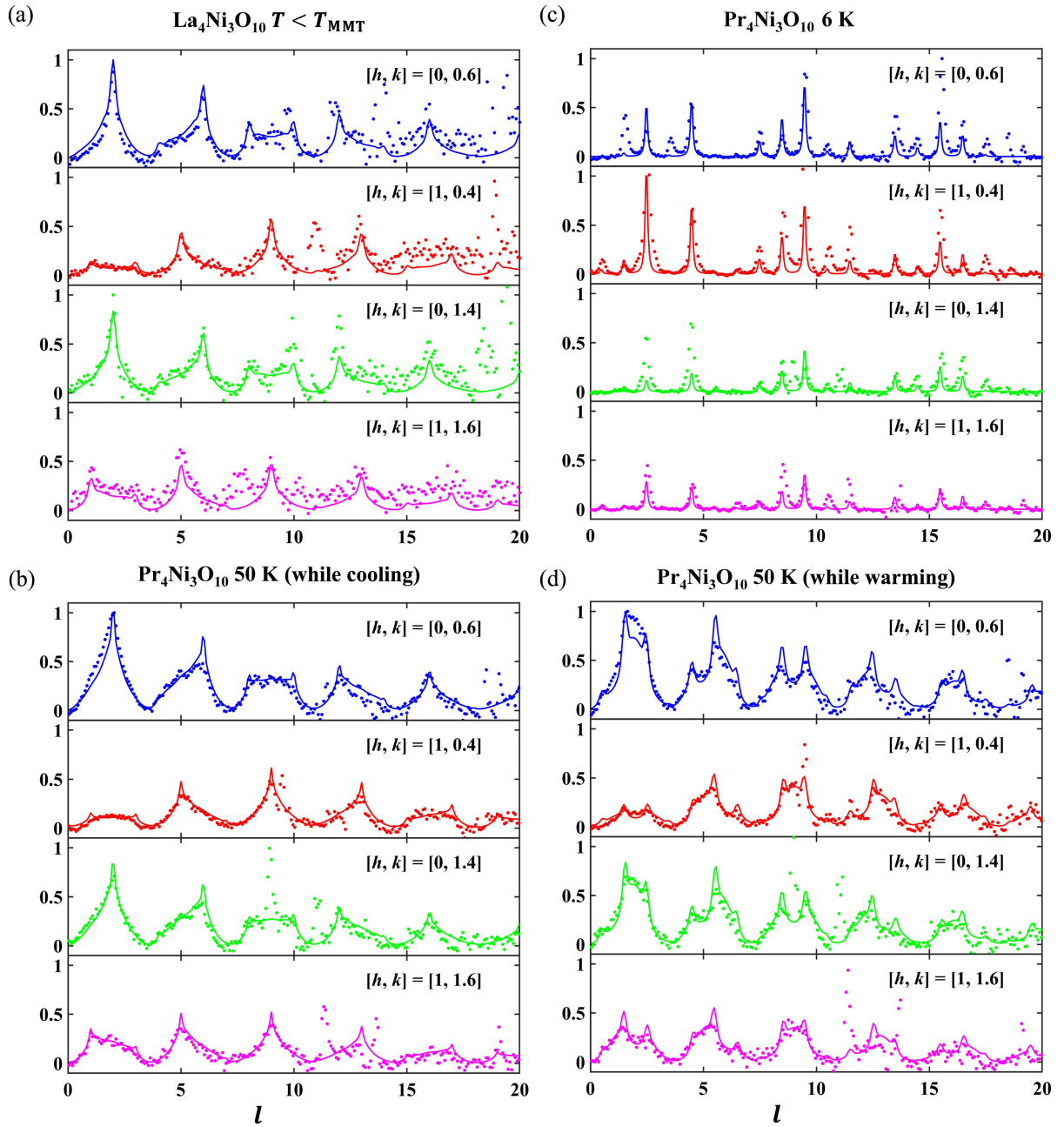


FIG. 4. Comparison of neutron data (symbols) and the corresponding optimized magnetic models (solid curves). (a)  $\text{La}_4\text{Ni}_3\text{O}_{10}$  data collected at  $T < T_{\text{MMT}}$ , (b)  $\text{Pr}_4\text{Ni}_3\text{O}_{10}$  data at 50 K measured while cooling from 200 K, (c)  $\text{Pr}_4\text{Ni}_3\text{O}_{10}$  data collected at base-temperature, and (d)  $\text{Pr}_4\text{Ni}_3\text{O}_{10}$  data measured at 50 K after warming from base temperature (approximately 6 K). Because of the temperature-independent nature of the structure factors below  $T_{\text{MMT}}$  for  $\text{La}_4\text{Ni}_3\text{O}_{10}$  [see Fig. 3(d)], all the low-temperature data (5 and 50 K warming and cooling) are combined in panel (a). Each panel shows line cuts of 3D scattering data along  $l$  for four different combinations of  $h \pm 0.1$  and  $k \pm 0.1$ :  $[0, 0.6]$ ,  $[1, 0.4]$ ,  $[0, 1.4]$ , and  $[1, 1.6]$ . The data measured at 200 K ( $>T_{\text{MMT}}$ ) are treated as the nonmagnetic background and subtracted (see Supplemental Material Sec. I, Ref. [9]).

this operation. The sequence of stacking of the six individual Ni layers which compose a magnetic unit cell can thus be expressed as a series of multiplicative factors denoted by  $[1, 0, -1]$ , meaning the top and bottom layers of a trilayer are  $\pi$  out of phase (i.e., antiferromagnetically aligned) and the middle layer lies on a node. This quasi-2D structure is illustrated in Fig. 6(a).

The more complete data for  $\text{La}_4\text{Ni}_3\text{O}_{10}$  collected on CORELLI now allow for a more thorough determination of the correlations. First, we find that the direction of spin polarization in the top and bottom layers lies along  $\mathbf{a}$ , perpendicular to the direction of propagation of the SDW,  $\mathbf{q}_{\text{SDW}} \perp \mathbf{a}$ . Symmetry demands that the ordered moments of the middle layer vanish, unless the arrangement of spins is

noncollinear. We test for this latter possibility and find that, within the sensitivity of the data, there is an upper bound on any noncollinear-ordered moment in the middle layer of approximately 60% that of the ordered moment in the outer planes ( $M_{\text{Ni}_B} < 0.6M_{\text{Ni}_A}$ ). For convenience, we set the ordered moment of the middle layer to be zero in the rest of the numerical analysis.

Given this framework, we then consider a model (see Supplemental Material Sec. III, Ref. [9]) consisting of a superposition of correlated trilayers of varying stacking length  $L_n$ , where  $L_n$  refers to the number of trilayers that are correlated along  $c$  (each possessing the series of multiplicative phase factors  $[1, 0, -1]$ ); that is,  $L_1$  refers to a single trilayer uncorrelated with its neighbors, whereas  $L_2$  refers to two (and only two) correlated trilayers. Thus, the intensity can be considered to be proportional to  $\sum_n \rho(L_n) [I(L_n)/L_n]$ , where  $\rho(L_n)$  represents the probability that a given layer lies within a correlated block of size  $n$  trilayers, and  $I(L_n)$  represents the corresponding structure factor [note that  $I(L_n)$  is proportional to  $L_n$ ]. The fitting of  $\rho(L_n)$  allows for optimization of the observed peak shapes, which are complex and contained both broad (captured by low  $n$ ) and narrow components (captured by high  $n$ ). The best fit, as shown in Fig. 4(a), consists of a rapidly decaying  $\rho(L_n)$  with increasing  $n$ —as would be expected for quasi-2D order—combined with a nonzero minority contribution captured by a component with larger  $n$  which breaks the trend of decay. This model implies what appears to be an inhomogeneous mixture in which the majority of the SDW order is short ranged (with low  $n$ ) but for which a minority long-range-ordered component (with high  $n$ ) coexists. Let us note that this latter minority component can be captured by any sufficiently high value of  $n$  that approaches the resolution limit of the spectrometer, and so the exact value of  $n$  should not be considered significant. The resulting probability distribution is shown in Fig. 5 with further details of the peak fitting described in the Supplemental Material (Fig. S11 and surrounding text). Application of the same approach for the IntC state of  $\text{Pr}_4\text{Ni}_3\text{O}_{10}$  also leads to a reasonable fit of the observed  $l$  dependence [see Fig. 4(b)], and a rapidly decaying  $\rho(L_n)$ , with a similar cutoff ( $n > 3$  in this case), consistent with the quasi-2D structure and polarization along  $a$  found for  $\text{La}_4\text{Ni}_3\text{O}_{10}$ . The outcome of this analysis confirms the qualitative picture developed in Ref. [14] for this intermediate-temperature structure, which is shared between La- and  $\text{Pr}_4\text{Ni}_3\text{O}_{10}$  (on cooling), but establishes a more quantitative foundation for how the trilayer building blocks correlate with their neighbors.

We now turn to the low-temperature behavior of  $\text{Pr}_4\text{Ni}_3\text{O}_{10}$ . To construct a SDW model for the LowT phase, we consider a magnetic unit cell of twice the nuclear unit cell along  $c$  with periodic boundary conditions since the magnetic correlations clearly span many nuclear cells along  $c$ , and Bragg peaks are located at half-integer

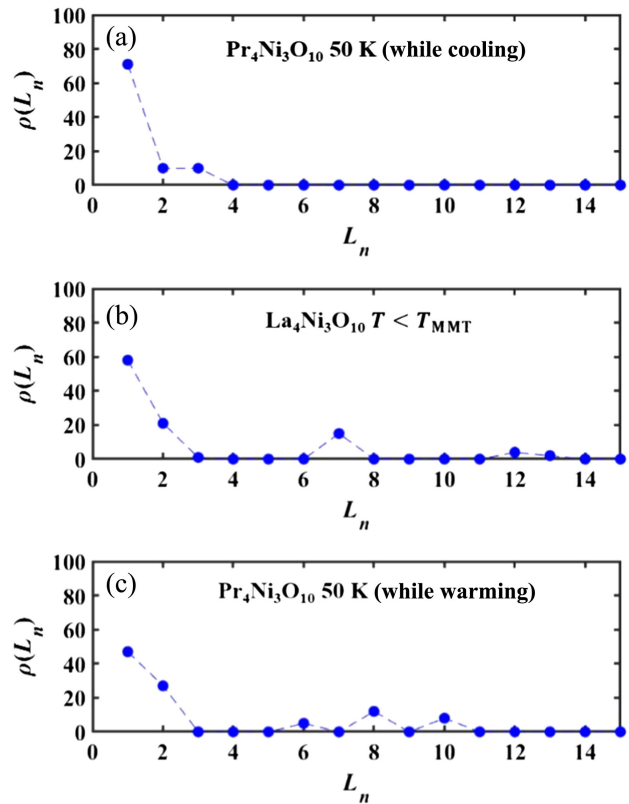


FIG. 5. The probability distributions  $\rho(L_n)$  as a function of the stacking length ( $L_n$ ) obtained by fitting neutron diffuse scattering datasets. The extracted  $\rho(L_n)$  for (a) the  $\text{Pr}_4\text{Ni}_3\text{O}_{10}$  dataset measured at 50 K after cooling from higher temperatures, (b) the  $\text{La}_4\text{Ni}_3\text{O}_{10}$  dataset measured below  $T_{\text{MMT}} \approx 148$  K, and (c) the  $\text{Pr}_4\text{Ni}_3\text{O}_{10}$  dataset measured at 50 K after warming from the base temperature are shown.

positions [Fig. 3(c)]. In the subsequent section, we construct a phenomenological model to explain this cell doubling. As we show above, resonant x-ray scattering (RXS) unambiguously shows that Pr contributes to the magnetic scattering. Thus, an SDW model for the low-temperature phase must explicitly account for this contribution. Indeed, attempts to fit the low-temperature data using a Ni-only model fail (see Supplemental Material Sec. IV, Fig. S12, Ref. [9]). Note that as shown in Fig. 1(a), the basal planes of Pr atoms can be subdivided into two inequivalent sites marked as  $A$  and  $B$ . The planes consisting of Pr  $A$  sites lie between Ni trilayers, while the planes consisting of Pr  $B$  sites lie within the Ni trilayers. Since we see strong magnetic peaks along  $c$  with the same in-plane incommensurate wave vectors ( $h, k$ ) as found above the dimensional crossover, the Pr layers are treated as an induced SDW, with the same in-plane periodicity as the Ni layers. However, the SDW polarization (moment orientation)  $\sigma_{\text{Pr}}$  for each Pr layer, the SDW polarization  $\sigma_{\text{Ni}}$  for Ni layers, and the amplitude of SDWs for Pr  $A$  and  $B$  sites ( $M_{\text{Pr}_A}$ ,  $M_{\text{Pr}_B}$ ) are refined independently using IOP. Furthermore, not only is the neutron structure factor



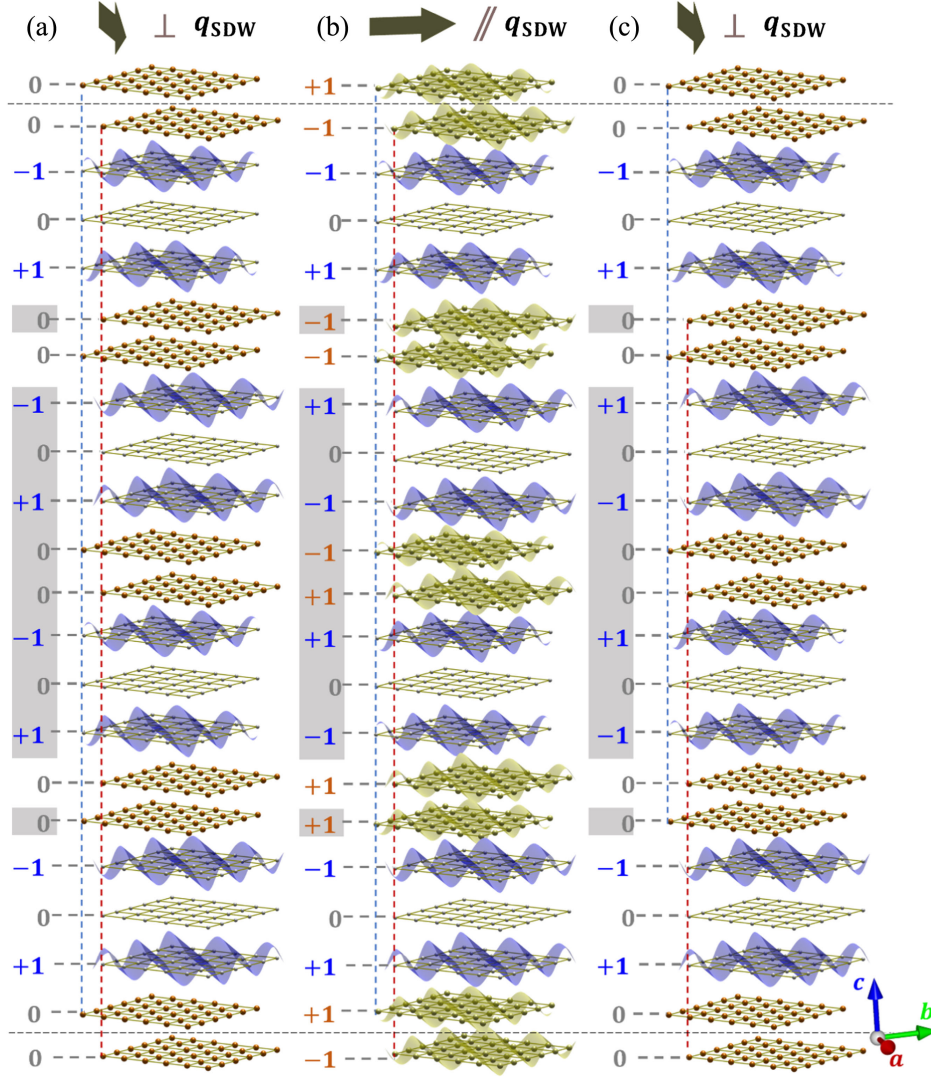


FIG. 6. The optimized magnetic models for (a) the intermediate-temperature phase ( $T_f < T < T_{\text{MMT}}$ ) while cooling from the paramagnetic phase IntC, (b) the low-temperature phase ( $T < T_f$ ) LowT, and (c) the intermediate-temperature phase ( $T_f < T < T_{\text{MMT}}$ ) while warming from the low- $T$  phase IntW. The corresponding SDWs are plotted in the orthorhombic  $a$ - $b$  plane. Note that only Ni A and Pr A layers are shown since moments on Ni B and Pr B are taken as zero. The SDWs shown here are depicted in the same convention as in Ref. [14]. The gray color boxes highlight the in-plane twist operation (twist angle  $\varphi$ ) on the polarization vectors with respect to the rest of the layers (see Sec. IV for more details). Among these three phases, only the LowT phase is long-range ordered, and the other two phases have distributions of stacking lengths as discussed in the text.

considered, but also  $I(\mathbf{Q}_{\text{RXS}}, \Psi)$  from the RXS experiment is included in the optimization. This optimization process concludes that the induced moment on the Pr B site is  $M_{\text{Pr}_B} < 0.1M_{\text{Ni}_A}$ , which is negligibly small. We note that other authors have postulated that the Pr B site has a nonmagnetic  $4f$  crystal-field ground state [12] based on the levels of perovskite  $\text{PrNiO}_3$  [20]. Additionally, the induced moment for the Pr A site is found to be within  $\pm 10\%$  of that of the outer-layer Ni A sites (see Sec. VID). As we illustrate in Fig. 6(b), for the best fit to the LowT data, both  $\sigma_{\text{Ni}}$  and  $\sigma_{\text{Pr}}$  lie parallel rather than perpendicular to  $\mathbf{q}_{\text{SDW}}$  as we find in the intermediate phase. We propose below that this is due to a dominant Pr single-ion

anisotropy that couples through exchange to the neighboring Ni sublattice [see Sec. IV and Eq. (1)]. The corresponding  $I^{\text{sim}}(\mathbf{Q})$  is shown in Fig. 4(c).

We note that additional peaks are observed at values of  $k$  in the low-temperature state that are not observed in the IntW or IntC phases. These peaks can be seen in Fig. 3(a), occurring at  $k = 0.4$  and  $k = 1.6$  corresponding to the addition of an odd integer to the values of  $k$  at which magnetic peaks are observed in the IntW and IntC states, thus reflecting an additional broken symmetry. Although they are considerably weaker than the primary peaks that we model, they are considerably stronger than those generated by the solution proposed above. There are a



number of variables that can contribute to such a broken symmetry such as spin canting, a much larger monoclinic structural distortion than indicated by the structural refinement, and additional SDW phase shifts between the layers. In Supplemental Material Sec. VII, Ref. [9], we show that these peaks can be satisfactorily modeled as arising from magnetic space-group operations that act on the components of the Pr and Ni moments canted away from  $\mathbf{b}$ . However, given the additional degrees of freedom that can be invoked to generate these peaks, there is no unique solution based on the data we have. Future polarized neutron-scattering measurements could better determine the cant angles and identify whether any additional phase shifts exist or not. We remark that the existence of canting is not surprising. Canting is almost certainly due to the Dzyaloshinskii-Moriya antisymmetric exchange that is prevalent in transition-metal oxides, particularly those with low symmetry as in the present case.

Another issue concerns the potential influence of stacking faults, which commonly occur in Ruddlesden-Popper materials. Such defects could cause a “phase slip” [21,22], thereby disturbing the coherence of the charge and spin density waves along the  $\mathbf{c}$  axis, and potentially lead to intensity at otherwise forbidden or weak reflections. We do not know the quantity of stacking faults in our crystals, but given the relatively narrow linewidths observed in the low-temperature state, we infer that the density of stacking faults is likely inconsequential since such faults would also lead to linewidth broadening.

Next, we turn to the IntW phase of  $\text{Pr}_4\text{Ni}_3\text{O}_{10}$ . Although the overall modulation is similar to the IntC state, significant differences are found in the diffuse peak profiles, indicating that a different set of correlations dominate the scattering upon warming. As we illustrate in Fig. 6(c), a similar SDW model with a different stacking pattern of the four trilayers in the doubled unit cell along  $\mathbf{c}$  [1, 0, -1; 1, 0, -1; -1, 0, 1; -1, 0, 1] is found to fit the data better (see Supplemental Material Sec. III, Ref. [9]). Furthermore, the conditions  $\sigma_{\text{Ni}} \perp \mathbf{q}_{\text{SDW}}$  and  $M_{\text{Ni}_B} < 0.6M_{\text{Ni}_A}$  found for IntC apply to IntW as well, and a composite model that includes a series of stacking lengths ( $L_n < 16$ ) with a specific  $\rho(L_n)$  is needed to fit the profiles. The  $\rho(L_n)$  derived from the fitting supports a higher-density distribution of extended intertrilayer correlations with  $L_n \geq 6$  (see Fig. 5), which lends quantitative justification to the claim above that the low-temperature, long-range  $\mathbf{c}$ -axis-ordered SDW that results from Ni-3d to Pr-4f exchange pathways is imprinted on the Ni sublattice and retains this imprint even when the Pr sublattice is no longer ordered, and the 3d-4f coupling is thus quenched.

To summarize the key results presented above: (1) a quasi-2D-ordered SDW in the Ni trilayers with  $\sigma_{\text{Ni}} \perp \mathbf{q}_{\text{SDW}}$  induces a corresponding SDW below  $T_f \approx 26$  K in the Pr blocks between the trilayers; (2) coincident with this induced order, a quasi-2D to 3D bootstrapped crossover

leads to long-range 3D order along the  $\mathbf{c}$  axis for both Ni and Pr sublattices, a doubling of the magnetic unit cell along  $\mathbf{c}$ , and a rotation of the moment such that  $\sigma \parallel \mathbf{q}_{\text{SDW}}$ ; (3) upon warming, the Pr sublattice loses long-range order at  $T_f$ , while the Ni sublattice retains a “memory” of the low- $T$  ordering, albeit on a greatly reduced out-of-plane length scale, until the CDW and SDW order simultaneously melt at  $T_{\text{MMT}} \approx 6T_f$ .

#### IV. DISCUSSION

Having established the temperature dependence of the magnetic phase behavior and presented models for both the low- and intermediate-temperature phases consistent with the diffraction data, we now present a phenomenological, microscopic framework that explains all elements of this unusual behavior.

At  $T_{\text{MMT}}$ ,  $\text{Pr}_4\text{Ni}_3\text{O}_{10}$  simultaneously develops a CDW and SDW. The CDW correlation length exceeds that of the SDW, which lacks long-range SDW order along  $\mathbf{c}$  due to the frustrated geometry of the coupling between the trilayers and a weak intertrilayer exchange expected because of the distance between trilayer blocks. As the temperature is further lowered, the ordering of nickel moments induces a moment on Pr A sites. Because of the lack of mirror symmetry of magnetic Ni sites across the Pr planes, an exchange field will be experienced by the Pr A atoms arising from the Ni SDW order. The local magnetic field on Pr atoms scales with the local moments on nearby nickel sites, and this lifts the Pr A sites out of the crystal-field singlet state (see discussion of the crystal-field levels in Supplemental Material Sec. VI, Ref. [9]) and imparts a SDW onto them with the same basal plane periodicity as the Ni SDW. For this reason, the  $k$  component of the magnetic wave vector is the same in both the low- and intermediate-temperature phases. We conjecture that the Pr B sites lack an induced moment due to the local crystal field inside a perovskitelike trilayer, akin to  $\text{PrNiO}_3$ , for which  $\text{Pr}^{3+}$  remains non-magnetic [12,20].

For a more quantitative phenomenological understanding, we construct the following minimal magnetic Hamiltonian:

$$\begin{aligned}
 H = & \sum_{n=1,2} \sum_{\langle i,j \rangle_n} \sigma_i \cdot J_n \cdot \sigma_j + M_{\text{Pr}_A} \sum_{\langle i,j \rangle_3} \sigma_i \cdot J_3 \cdot \sigma_j \\
 & + M_{\text{Pr}_A}^2 \sum_{\langle i,j \rangle_4} \sigma_i \cdot J_4 \cdot \sigma_j - DM_{\text{Pr}_A}^2 \sum_{\text{Pr}_A} (\sigma_i \cdot \hat{b})^2 \\
 J_1 = & \begin{bmatrix} J_a & 0 & 0 \\ 0 & J_b & 0 \\ 0 & 0 & J_c \end{bmatrix}, & J_2 = & \begin{bmatrix} J_d & 0 & 0 \\ 0 & J_d & 0 \\ 0 & 0 & J_d \end{bmatrix}, \\
 J_3 = & \begin{bmatrix} J_e & 0 & 0 \\ 0 & J_f & 0 \\ 0 & 0 & J_g \end{bmatrix}, & J_4 = & \begin{bmatrix} J_h & 0 & 0 \\ 0 & J_h & 0 \\ 0 & 0 & J_h \end{bmatrix} \quad (1)
 \end{aligned}$$

where  $\sigma_i$  is the SDW polarization vector for the  $i$ th basal plane, and the exchanges  $J_n$  are defined as marked in Fig. 1(c):  $J_1$  and  $J_2$  link Ni ions, and  $J_3$  and  $J_4$  link Ni to Pr and Pr to Pr, respectively, with  $M_{\text{Pr}}$  defined relative to the Ni  $A$  site moments. Note that exchange tensors are defined in a coordinate system where the  $x$  axis is parallel to the crystallographic direction  $\hat{a}$ . Only  $J_1$  and  $J_3$  are made anisotropic due to the anisotropic nature of the superexchange pathway [see Fig. 1(c) and Supplemental Material Table S3, Ref. [9]], with  $J_1$  enforcing the anti-phasing between the outer Ni layers. Because of the long interaction distance associated with  $J_2$  and  $J_4$ , we treat these as isotropic. In the intermediate phases,  $M_{\text{Pr}_A} = 0$ , and only the  $J_1$  and  $J_2$  exchanges remain. The exchange parameters should follow simple conditions  $J_a > J_b, J_c \geq 0$  to satisfy  $\sigma_{\text{Ni}} \perp \mathbf{q}_{\text{SDW}}$  and  $J_d > 0$  to yield the IntC stacking order of the trilayers as the lowest in energy. The experimental observation that  $\sigma_{\text{Ni}}$  lies along  $\mathbf{a}$  can be understood from simple considerations of octahedral rotation patterns discussed by Koshibae *et al.* [23]. Because of the anisotropic oxygen environment surrounding Pr  $A$ , we introduce the last term to account for possible single-ion anisotropy (SIA) with strength  $D$  and easy axis along  $\hat{b}$ . Further details can be found in Supplemental Material Sec. V, Ref. [9].

As we show in Fig. 6(b), the  $\sigma$  for the Pr layers ( $A$  sites) are experimentally found to be opposite the nearest Ni layer in the same sublattice in the LowT phase. Thus, the

$J_3$  exchange interaction should be antiferromagnetic. The  $J_4$  exchange connects two consecutive Pr  $A$  layers through a nonmagnetic Pr  $B$  layer in the same sublattice, and it should be ferromagnetic ( $J_h < 0$ ) with the condition  $2|J_d| < |J_h|$  to stabilize the experimentally observed stacking pattern of the LowT phase with a doubled  $c$  axis in its magnetic structure. Finally, the easy-axis SIA along  $\hat{b} \parallel \mathbf{q}_{\text{SDW}}$  is introduced to enforce the LowT phase polarization along the SDW propagation direction assuming the  $J_3$  tensor follows the same anisotropic condition as  $J_1$  ( $J_e > \{J_f, J_g\} \geq 0$ ). Alternatively, the same LowT structure can be stabilized without SIA under the condition  $J_f > \{J_e, J_g\} \geq 0$  (see Supplemental Material Fig. S17, Ref. [9]).

The difference between the two SDW models for IntC and IntW is that the SDW polarization for half of the basal planes has flipped [compare the gray boxes in Fig. 6(a) to those of Figs. 6(b) and 6(c)]. The IntCIntW structure should be the global minimum in this temperature regime since it is experimentally found to be the most favorable while cooling from high temperatures. Thus, the structure is a metastable state protected by a sufficiently high-energy barrier. An expression can be derived from Eq. (1) for the magnetic energy of the system connecting two solutions in configurational space via a continuous transformation,

$$\begin{aligned}
 E \propto & -2[J_a[\cos^2(\Theta + \varphi) + \cos^2(\Theta)] + J_b[\sin^2(\Theta + \varphi) + \sin^2(\Theta)]] \\
 & + 2J_d[1 - \cos(\varphi)] - 4M_{\text{Pr}_A}[J_e[\cos^2(\Theta + \varphi) + \cos^2(\Theta)] + J_f[\sin^2(\Theta + \varphi) + \sin^2(\Theta)]] \\
 & - 4J_h M_{\text{Pr}_A}^2 \cos(\varphi) - 8DM_{\text{Pr}_A}^2[\sin^2(\Theta + \varphi) + \sin^2(\Theta)].
 \end{aligned} \tag{2}$$

Here,  $\Theta$  and  $\varphi$  are, respectively, the global in-plane rotation of  $\sigma$  with respect to the  $\mathbf{a}$  axis and the relative rotation of  $\sigma$  between adjoining layers (gray boxes in Fig. 6) that for  $\varphi = \pi$  takes IntW into IntC (see Supplemental Material Fig. S15, Ref. [9]). In other words, the subset of moments delineated by the gray boxes in Fig. 6 twists with respect to the other moments (which do not rotate) by an angle  $\varphi$  within the  $\mathbf{a}$ - $\mathbf{b}$  plane. For illustration, when  $\varphi = 0$ ,  $\sigma$  is perpendicular to  $\mathbf{q}_{\text{SDW}}$  for  $\Theta = 0$  and  $\sigma$  is parallel to  $\mathbf{q}_{\text{SDW}}$  for  $\Theta = \pi/2$ . Figure 7 shows the energy landscape for a potential choice of exchange parameters as a function of  $\varphi$  and  $M_{\text{Pr}_A}$  at a fixed  $\Theta$ , where the energy is minimized for each panel. Note that the energy is minimized for  $\Theta = 0$  for all the presented  $M_{\text{Pr}_A}$  values except for  $M_{\text{Pr}_A} = 1$ , where it takes the value  $\pi/2$ . The generalized case of finite  $\Theta$  can be found in Supplemental Material Sec. V, Ref. [9]. As shown in the top panel of Fig. 7, the global minimum for this Hamiltonian is at  $\varphi = 0$  for  $\Theta = 0$  (IntC). We check the robustness of this solution under the sensitivity analysis given in Supplemental Material Fig. S15, Ref. [9].

The induced moment on the Pr  $A$  site is temperature dependent, as observed in the RXS experiment [see Supplemental Material Fig. S7(b), Ref. [9]]. To understand the metastable trapping in the intermediate temperatures upon heating from base temperature, the energy landscape is generated by first increasing  $M_{\text{Pr}_A}$  (a proxy for temperature) and then decreasing to zero, as shown in Fig. 7 from the top panel to the bottom. As  $M_{\text{Pr}_A}$  increases as a consequence of decreasing temperature, the energy landscape evolves, and after a certain value (in this case,  $M_{\text{Pr}_A} \approx 0.5$ ), the global minimum is no longer at  $\varphi = 0$  but  $\varphi = \pi$ , which is the IntW configuration with low- $T$  stacking. Increasing  $M_{\text{Pr}_A}$  further will drive the system to the LowT phase (see Supplemental Material Fig. S16, Ref. [9]). On raising  $T$  (decreasing  $M_{\text{Pr}_A}$ ), the system will be moved to the  $\varphi = \pi$  configuration and become trapped by the energy barrier between the  $\varphi = 0$  and  $\pi$  configurations. Apparently, this barrier is sufficiently high in practice to protect the metastable IntW state until all order vanishes at  $T_{\text{MMT}}$ . Our minimal model thus captures all

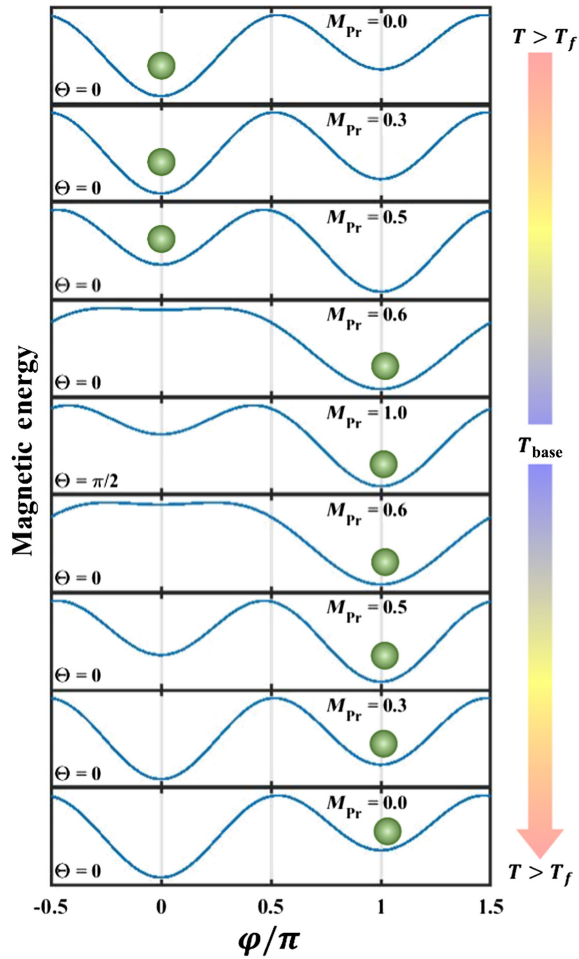


FIG. 7. Energy landscape of the two-unit-cell magnetic system in configurational space parametrized by the in-plane twist angle  $\varphi$ , with the twisted spins delineated by the gray boxes in Fig. 6. The exchange parameters used here are  $J_a = 1$ ,  $(J_b/J_a) = 0.5$ ,  $(J_c/J_a) = 0$ ,  $(J_d/J_a) = 0.1$ ,  $(J_e/J_a) = 0.5$ ,  $(J_f/J_a) = 0.25$ ,  $(J_g/J_a) = 0$ ,  $(J_h/J_a) = -0.3$ , and  $(D/J_a) = 0.5$ . Note that  $\varphi = 0$  and  $\pi$  correspond to the IntC and IntW structures shown in Fig. 6, respectively. The energy landscapes are derived from Eq. (2) by varying the induced moment on the Pr A site. As shown in Fig. 1(f), the induced Pr moment increases with decreasing temperature. In the same notion,  $M_{Pr}$  increases from (top) 0 to (middle) 1 and decreases again back to (bottom) 0 to yield the observed thermal hysteresis. The green color markers are a guide to show the stable configuration of the system at a particular step in the process.

experimentally observed elements, including the rotation of  $\sigma$ , the metastability of the IntW phase, and the thermal hysteresis of the Ni-centered SDW.

Let us consider the case of  $\text{Pr}_4\text{Ni}_3\text{O}_{10}$  within the context of other transition-metal oxides where both transition-metal and rare-earth sublattice magnetism are present. Considerable experimental work has been done on the rare-earth magnetism in layered cuprates, which is relevant here because certain cuprates such as  $\text{YBa}_2\text{Cu}_3\text{O}_{7-x}$  possess weak density wave order that appears to be related

to the Fermi-surface geometry, as suggested by quantum oscillation [24] and Fourier-STM studies [25]. In the 1-2-3, 2-4-8, and 2-4-7 cuprates, commensurate antiferromagnetic rare-earth ordering is observed in the materials containing doubly degenerate rare-earth  $4f$  crystal-field states, the ordering occurring at low temperatures (of order 1 K) due to dipole-dipole interactions [26]. This ordering is exemplified by  $\text{ErBa}_2\text{Cu}_3\text{O}_7$  ( $T_N = 0.618$  K) where the Er sublattice behaves as a realization of the 2D  $S = 1/2$  Ising model [26]. Well below  $T_N$ , i.e.,  $\ll 1$  K, the rare-earth sublattice can evolve from 2D to 3D as even a weak  $c$ -axis coupling becomes magnified by the sheer number of interacting spins within a domain to lower the energy [26]. Similar behavior is found in  $\text{Er}_2\text{Ba}_4\text{Cu}_8\text{O}_{16}$  [27]. The extremely low temperatures at which this latter effect occurs points to a different mechanism than that described here. The single-layer  $T'$  2-1-4 cuprate,  $\text{Nd}_2\text{CuO}_4$  provides an interesting comparison to  $\text{Pr}_4\text{Ni}_3\text{O}_{10}$ . The Cu spins develop antiferromagnetic order at 245 K; a spin reorientation occurs at approximately 30 K, followed by an induced moment on the Nd sublattice [4]. The reorientation and the smeared nature of the low-temperature order parameter are reminiscent of the induced moment in  $\text{Pr}_4\text{Ni}_3\text{O}_{10}$ . However, the dimensional crossover and imprinting effects have not been reported in any cuprates that we are aware of. In nickelates, neutron diffraction shows that the Ni sublattice in  $\text{Pr}_2\text{NiO}_4$  orders antiferromagnetically at 325 K (where the crystal symmetry is Bmab) with moments along the  $a$  axis, as we find in  $\text{Pr}_4\text{Ni}_3\text{O}_{10}$  [3,23]. The low-temperature magnetic behavior of  $\text{Pr}_2\text{NiO}_4$  is more complex than that of  $\text{Pr}_4\text{Ni}_3\text{O}_{10}$ , including spin reorientations and the emergence of a ferromagnetic component allowed by a structural phase transition at 115 K to  $P4_2/nm$ . Below 40 K, an increase in magnetization has been associated with partial ordering of  $\text{Pr}^{3+}$ , with neutron-diffraction intensities attributed to polarization of  $\text{Pr}^{3+}$  by the exchange field of the ordered Ni sublattice. However, neither a quasi-2D to 3D crossover nor feedback to the Ni sublattice has been reported in  $\text{Pr}_2\text{NiO}_4$ . It is worth noting that non-Kramers  $\text{Pr}^{3+}$  in both  $\text{Pr}_2\text{NiO}_4$  and in  $\text{Pr}_4\text{Ni}_3\text{O}_{10}$  should be in a singlet ground state due to their low site symmetry. Thus, a magnetic transition on the Pr sublattice of  $\text{Pr}_4\text{Ni}_3\text{O}_{10}$ , as proposed by Rout *et al.* [12], seems unlikely (see Supplemental Material Sec. VI, Ref. [9]).

## V. SUMMARY

In summary, we use a combination of neutron diffraction and resonant x-ray diffraction to unveil the evolution of the SDW, which is coupled to a CDW, in  $\text{Pr}_4\text{Ni}_3\text{O}_{10}$ . Detailed models of the magnetic ordering in all phases are presented, and a microscopic model of exchange interactions is proposed to explain the phase behavior and the metastability of the intermediate-temperature state on warming. The first striking experimental finding from this work is



that the dimensionality of the magnetic correlations in the SDW is modified as a function of the temperature by the interaction of the Pr-4*f* moments with the Ni-3*d* moments. Above 26 K, the Ni sublattice orders in quasi-2D, with weak correlations *c* along enforced by geometric frustration. Below 26 K, a new Pr-centered order develops, whose temperature dependence suggests an induced-moment effect from the Ni sublattice on what would otherwise be non-magnetic, singlet-state ions. Once a finite-ordered moment is induced on Pr<sup>3+</sup>, a new exchange pathway opens along *c*, breaking the frustration and leading to 3D order of both sublattices. Given that these cascading events originate from the order of the Ni cations themselves, we describe this mechanism as bootstrapping (a phenomenon known colloquially in physics as “pulling oneself up by the bootstraps”). Remarkably, the imprint of this effect on the nickel sublattice survives a reheating back into the intermediate-temperature phase and disappears only if the temperature is increased above  $T_{\text{MMT}}$ , where the CDW or SDW melts. Surprisingly, we see no evidence that the CDW is modified by the dramatic evolution in the SDW, despite the obvious coupling between the SDW and CDW [Fig. 1(f)]. Specifically, we observe no significant difference in the in-plane wave vector or the line shape of the CDW between the intermediate- and low-temperature states (see Supplemental Material Fig. S6, Ref. [9]). It is possible that such an impact in the charge sector is too subtle for the diffraction probes used here, and we might expect to find a spectroscopic signature of the coupling using other probes.

As we mention in the Introduction, exchange interactions between 3*d* and 4*f* moments play a prominent role in other contexts, including multiferroicity [1] and topological transport phenomena [2], and examples of 4*f* to 3*d* influence, while rare, are also known. Because of this generality, it would be surprising if Pr<sub>4</sub>Ni<sub>3</sub>O<sub>10</sub> were a singular example of the phenomena described here, nor would the bootstrapping effect need to be confined to the magnetic sector due to the strong coupling among structural, electronic, and magnetic degrees of freedom commonly found in low-dimensional quantum materials. Along this line, we note that the substitution of Pr cations into YBCO has recently been claimed to precipitate a 3D charge-ordered state due to hybridization of the Pr-4*f* states with the oxygen-2*p* states [28]. Although this occurs in the charge sector and does not yield a temperature-dependent crossover as we see here, it provides another example where rare-earth cations can be used to control the dimensionality of density waves.

We conclude by noting that the general problem of understanding and manipulating intertwined order parameters associated with density waves is widely recognized as a frontier challenge in quantum materials [29,30], with relevance to our understanding of, for example, high-temperature superconducting cuprates [31–33], twisted-bilayer graphene [34,35], and superfluid <sup>4</sup>He [36,37].

We hope that the interesting case presented here of coupled rare-earth and transition-metal SDWs interacting through reciprocal 3*d*-4*f* and 4*f*-3*d* electron interactions will inspire further work in layered oxides to probe and understand on a quantitative basis the interactions that underlie such behaviors, including dimensional crossover phenomena.

## VI. METHODS

### A. Sample growth and characterization

A description of the growth of the Pr<sub>4</sub>Ni<sub>3</sub>O<sub>10</sub> and La<sub>4</sub>Ni<sub>3</sub>O<sub>10</sub> crystals employed in this study, as well as the electrical transport characterization of Pr<sub>4</sub>Ni<sub>3</sub>O<sub>10</sub>, can be found in our previous report [10].

### B. Resonant x-ray scattering

Synchrotron x-ray single-crystal diffraction measurements were performed at Sector 6-ID-B at the Advanced Photon Source, Argonne National Laboratory. The resonant measurements are made with incident x-ray energies around the Pr *L*<sub>2</sub> edge at 6.439 keV and the Ni *K* edge at 8.333 keV. For the former measurements, a polarization analyzer in the  $\sigma$ - $\pi'$  configuration with the vertical scattering geometry was used. The magnetic reflection  $Q_{\text{RXS}} = (0, -0.617, 9.5)$  is measured along [00*l*] as a function of the azimuthal angle ( $\Psi$ ) at a fixed temperature of 5 K.

### C. Neutron scattering

Elastic-neutron-scattering experiments were carried out on a Pr<sub>4</sub>Ni<sub>3</sub>O<sub>10</sub> crystal at the MACS triple-axis spectrometer and the SPINS triple-axis spectrometer [38], both located at the NIST Center for Neutron Research, Gaithersburg, MD. For both spectrometers, the incident and final neutron energies are fixed to be  $E_i = E_f = 5.0$  meV, and the harmonics are suppressed by beryllium filters. Further neutron investigations were performed on the same Pr<sub>4</sub>Ni<sub>3</sub>O<sub>10</sub> crystal as well as a single crystal of La<sub>4</sub>Ni<sub>3</sub>O<sub>10</sub> at the diffuse scattering spectrometer CORELLI, Spallation Neutron Source, Oak Ridge National Laboratory. CORELLI is a time-of-flight instrument where the elastic contribution is separated by a pseudo-statistical chopper [39]. The crystal was rotated through 360° with a step of 3° horizontally with a vertical angular coverage of  $\pm 28.5^\circ$  for the survey of the elastic and diffuse peaks in reciprocal space. A standard closed-cycle refrigerator accessible at the CORELLI beamline was used. The data were reduced using MANTID [40] and PYTHON scripts available at CORELLI.

### D. Density wave models and simulations

The neutron-scattering cross section for a given SDW model is calculated using

$$I(\mathbf{Q}) = \sum_{\alpha,\beta} \frac{g_\alpha g_\beta}{4} \left( \delta_{\alpha\beta} - \frac{\kappa_\alpha \kappa_\beta}{|\mathbf{Q}|^2} \right) \times S^{\alpha\beta}(\mathbf{Q}), \quad (3)$$



where  $g_{\alpha,\beta}$  are the  $g$  factors,  $\mathbf{Q} = \kappa_x \hat{x} + \kappa_y \hat{y} + \kappa_z \hat{z}$  is the wave-vector transfer in the scattering process,  $\alpha, \beta = x, y, z$  are the initial and final spin polarizations of the neutrons in Cartesian coordinates, and  $S^{\alpha\beta}$  is the neutron-scattering factor correlation function:

$$S^{\alpha\beta}(\mathbf{Q}) = \frac{1}{2\pi N} |S_{\mathbf{Q}}^{\alpha} S_{-\mathbf{Q}}^{\beta}| \quad (4)$$

with

$$S_{\mathbf{Q}}^{\alpha} = \sum_i F_i(\mathbf{Q}) \sigma_i^{\alpha} \times \cos(\mathbf{q}_{\text{SDW}} \cdot \mathbf{r}_i + \phi) e^{i\mathbf{Q} \cdot \mathbf{r}_i}. \quad (5)$$

Unlike in systems with localized magnetic moments, which are usually represented as  $S_i$  with fixed amplitude, here the effective moment per ion is decomposed into a cosine component  $\cos(\mathbf{q}_{\text{SDW}} \cdot \mathbf{r}_i + \phi)$  characterized by the SDW propagation vector  $\mathbf{q}_{\text{SDW}}$  and the SDW polarization  $\sigma_i^{\alpha}$  to capture both the itinerant (single harmonic) and localized (Ni-site-centered) behavior. The offset parameter  $\phi$  is considered constant (0 or  $\pi$ ) for all the basal planes in each orthorhombic sublattice shown in Supplemental Material Fig. S13, Ref. [9].  $F_i(\mathbf{Q})$  is the magnetic form factor of the  $i$  th magnetic site. To accurately account for the instrumentation effects,  $I(\mathbf{Q})$  is convoluted with a Lorentzian of FWHM =  $0.027 \text{ \AA}^{-1}$  estimated from the strong nuclear Bragg peaks.

Diffuse scattering contributions due to short-range ordering of Ni trilayers are calculated using  $L_n/2$  unit cells along  $c$  ( $L_n$  number of trilayers) and 2500 orthorhombic unit cells in the plane, which is equivalent to a total of  $15000 \times L_n$  Ni ions. The slight Bmab deviations of the outer-plane Ni  $A$  ions from their  $I4/mmm$  positions are taken into account, using atomic coordinates given in Ref. [10].  $I(\mathbf{Q})$  for simple combinations of  $L_n$  stackings are shown in Supplemental Material Fig. S9, Ref. [9].

For the purpose of optimization, each Ni trilayer is parametrized by three local rotation angles  $\alpha_{\text{Ni}_A}^n, \beta_{\text{Ni}_A}^n, \gamma_{\text{Ni}_B}^n$  ( $n = 1, 2, \dots$ ) and one global moment amplitude ( $M_{\text{Ni}} = M_{\text{Ni}_B}/M_{\text{Ni}_A}$ ) as described in Supplemental Material Fig. S8, Ref. [9]. In addition, the probability density for each stacking of length  $L_n$  is also refined for the models that allow multiple stackings to exist simultaneously. For each Ni trilayer, the conditions that the outer-layer polarizations  $\sigma_{\text{Ni}_A}$  are equal and opposite, and the middle-layer polarization  $\sigma_{\text{Ni}_B}$  is perpendicular to  $\sigma_{\text{Ni}_A}$ , are enforced.

From the initial optimization attempts using IntC data and simple SDW models that accommodate up to two types of stacking (see Supplemental Material Sec. III, Ref. [9]), we realize that the optimal solution lies at  $\alpha_{\text{Ni}_A}^n \approx \pi/2$ ,  $\beta_{\text{Ni}_A}^n \approx 0$ , or  $\pi$ ,  $M_{\text{Ni}} < 0.6$  and  $\gamma_{\text{Ni}_B}^n \in [0, 2\pi]$  (unrefinable for lower  $M_{\text{Ni}}$ ), and  $\{\alpha_{\text{Ni}_A}^n, \beta_{\text{Ni}_A}^n, \gamma_{\text{Ni}_B}^n, M_{\text{Ni}}\}$  is fixed to  $\{\pi/2, 0, 0, 0\}$  for longer-range SDW models with  $L_n$  up to 16 (here,  $M_{\text{Ni}}$  refers to the Ni  $B$  sites). For the SDW

models corresponding to the  $\text{Pr}_4\text{Ni}_3\text{O}_{10}$  IntC structure and  $\text{La}_4\text{Ni}_3\text{O}_{10}$  low- $T$  structure, the stackings follow the pattern  $\{[1, 0, -1], [1, 0, -1], [1, 0, -1], [1, 0, -1], \dots\}$  ( $[\dots]$  represents a single trilayer). In contrast, the  $\text{Pr}_4\text{Ni}_3\text{O}_{10}$  IntW model follows the pattern  $\{[1, 0, -1], [1, 0, -1], [-1, 0, 1], [-1, 0, 1], \dots\}$ . Note that stackings with  $L_n < 3$  are the same for both models. The refined probabilities as a function of  $L_n$  are given in Fig. 5.

For the purpose of calculating  $I(\mathbf{Q})$  for a long-range stacking of the SDW, a box of  $20 \times 20 \times 10$  nuclear unit cells, which is equivalent to a total of 224 000 magnetic ions including both Ni and Pr sites, is considered along with periodic boundary conditions.

In the low- $T$  data-fitting process, the conditions of outer Ni-layer polarizations within a trilayer block being equal and opposite, and the corresponding middle-layer polarization being perpendicular to the outer layers, are enforced. The magnetic unit cell is assumed to be doubled along  $c$  (see Fig. 6), with the parametrization referring to the bottom unit cell (see Supplemental Material Fig. S8, Ref. [9]). The induced SDWs for Pr are considered similar to the Ni layers (same  $\mathbf{q}_{\text{SDW}}$  and  $\phi$ , not  $\sigma$ ), which belong to the same sublattice as shown in Supplemental Material Fig. S13, Ref. [9]. However, each Pr layer is parametrized by two local rotation angles  $\alpha_{\text{Pr}_A}^n, \beta_{\text{Pr}_A}^n$  ( $n = 1, \dots, 8$ ) and two global amplitudes  $M_{\text{Pr}_A}, M_{\text{Pr}_B}$ —the magnetic moment of Pr  $A$  and  $B$  sites relative to the outer-layer  $\text{Ni}_A$  moment, respectively. The optimal region for the  $\text{Pr}_4\text{Ni}_3\text{O}_{10}$  LowT neutron and RXS data is found to be at  $M_{\text{Pr}_A} \approx 1, M_{\text{Pr}_B} \approx 0, \alpha_{\text{Pr}_A} = \pi, \beta_{\text{Pr}_A} = 0, \alpha_{\text{Ni}_A}^2 = \beta_{\text{Ni}_A}^2 = \beta_{\text{Ni}_A}^1 = 0$ , and  $\alpha_{\text{Ni}_A}^1 = \pi$ . Similarly, in diffuse scattering data fitting  $M_{\text{Ni}} < 0.6$  is found (i.e., Ni  $B$  sites). Since the Pr  $B$  site and middle-layer  $\text{Ni}_B$  moments are small, the corresponding parameters for their orientation ( $\gamma_{\text{Ni}_B}^1, \gamma_{\text{Ni}_B}^2, \alpha_{\text{Pr}_B}$ , and  $\beta_{\text{Pr}_B}$ ) are unconstrained and set to zero in the final solution shown in Fig. 4(c).

## E. Optimization

To quantify the uncertainty of the proposed SDW models, we apply the IOP explained in Ref. [41]. In the case of diffuse scattering data fitting, the direct distance between the experimentally measured  $[I^{\text{exp}}(\mathbf{Q})]$  and the calculated  $[I^{\text{sim}}(\mathbf{Q})]$  neutron structure factors  $\chi^2 = (1/N_{\mathbf{Q}}) \sum [I^{\text{exp}}(\mathbf{Q}) - I^{\text{sim}}(\mathbf{Q})]^2$  is employed as the cost function of IOP.

In the case of LowT data fitting, a composite cost combining neutron data and RXS data,

$$\chi^2 = \frac{1}{N_{\mathbf{Q}_P}} \sum_{\mathbf{Q}_P} [I^{\text{exp}}(\mathbf{Q}_P) - I^{\text{sim}}(\mathbf{Q}_P)]^2 + \frac{1}{N_{\Psi}} \sum_{\Psi} [I^{\text{exp}}_{\text{RXS}}(\mathbf{Q}_{\text{RXS}}, \Psi) - I^{\text{sim}}_{\text{RXS}}(\mathbf{Q}_{\text{RXS}}, \Psi)]^2, \quad (6)$$

where  $I_{\text{RXS}}$  is the Pr  $L_2$ -edge x-ray resonant scattering cross section at the wave vector  $\mathbf{Q}_{\text{RXS}} = [0, -0.6, 9.5]$  (see Supplemental Material Sec. II, Ref. [9] for details), and  $\mathbf{Q}_P$  represents the SDW neutron peaks.

### ACKNOWLEDGMENTS

This work is supported by the U.S. Department of Energy, Office of Science, Basic Energy Sciences, Materials Science and Engineering Division. Research at ORNL's SNS is sponsored by the Scientific User Facilities Division, Office of Basic Energy Sciences, U.S. Department of Energy. Use of the Advanced Photon Source at Argonne National Laboratory is supported by the U.S. Department of Energy, Office of Science, Office of Basic Energy Sciences, under Contract No. DE-AC02-06CH11357. Access to MACS is provided by the Center for High Resolution Neutron Scattering, a partnership between the National Institute of Standards and Technology and the National Science Foundation under Agreement No. DMR-1508249. J. Z. gratefully acknowledges financial support from the National Natural Science Foundation of China (Grant No. 12074219), the Qilu Young Scholars Program of Shandong University, and the Taishan Scholars Program of Shandong Province. The authors would like to thank an anonymous reviewer for suggesting comparisons to other  $3d$ - $4f$  backinteractions in multiferroics and nickelate heterostructures.

- [1] O. Prokhnenko, R. Feyerherm, M. Mostovoy, N. Aliouane, E. Dudzik, A. U. B. Wolter, A. Maljuk, and D. N. Argyriou, *Coupling of frustrated ising spins to the magnetic cycloid in multiferroic TbMnO<sub>3</sub>*, *Phys. Rev. Lett.* **99**, 177206 (2007).
- [2] Y. Taguchi, Y. Oohara, H. Yoshizawa, N. Nagaosa, and Y. Tokura, *Spin chirality, berry phase, and anomalous Hall effect in a frustrated ferromagnet*, *Science* **291**, 2573 (2001).
- [3] M. T. Fernandez-Diaz, J. Rodriguez-Carvajal, J. L. Martinez, G. Fillion, F. Fernandez, and R. Saez-Puche, *Structural and magnetic phase transitions in Pr<sub>2</sub>NiO<sub>4</sub>*, *Z. Phys. B* **82**, 275 (1991).
- [4] J. W. Lynn, I. W. Sumarlin, S. Skanthakumar, W. Li, R. N. Shelton, J. L. Peng, Z. Fisk, and S.-W. Cheong, *Magnetic ordering of Nd in (Nd, Ce)<sub>2</sub>CuO<sub>4</sub>*, *Phys. Rev. B* **41**, 2569 (1990).
- [5] S. Miyasaka, T. Yasue, J. Fujioka, Y. Yamasaki, Y. Okimoto, R. Kumai, T. Arima, and Y. Tokura, *Magnetic field switching between the two orbital-ordered states in DyVO<sub>3</sub>*, *Phys. Rev. Lett.* **99**, 217201 (2007).
- [6] J. Fujioka, T. Yasue, S. Miyasaka, Y. Yamasaki, T. Arima, H. Sagayama, T. Inami, K. Ishii, and Y. Tokura, *Critical competition between two distinct orbital-spin ordered states in perovskite vanadates*, *Phys. Rev. B* **82**, 144425 (2010).
- [7] M. Reehuis, C. Ulrich, K. Proke, S. Mat' A, J. Fujioka, S. Miyasaka, Y. Tokura, and B. Keimer, *Structural and magnetic phase transitions of the orthovanadates RVO<sub>3</sub> (R = Dy, Ho, Er) as seen via neutron diffraction*, *Phys. Rev. B* **83**, 064404 (2011).
- [8] M. Bluschke, A. Frano, E. Schierle, M. Minola, M. Hepting, G. Christiani, G. Logvenov, E. Weschke, E. Benckiser, and B. Keimer, *Transfer of magnetic order and anisotropy through epitaxial integration of 3d and 4f spin systems*, *Phys. Rev. Lett.* **118**, 207203 (2017).
- [9] See Supplemental Material at <http://link.aps.org/supplemental/10.1103/PhysRevX.13.041018> for supporting information.
- [10] J. Zhang, H. Zheng, Y. S. Chen, Y. Ren, M. Yonemura, A. Huq, and J. F. Mitchell, *High oxygen pressure floating zone growth and crystal structure of the metallic nickelates R<sub>4</sub>Ni<sub>3</sub>O<sub>10</sub> (R = La, Pr)*, *Phys. Rev. Mater.* **4**, 083402 (2020).
- [11] M. E. Lines, *Comparative studies of magnetism in KNiF<sub>3</sub> and K<sub>2</sub>NiF<sub>4</sub>*, *Phys. Rev.* **164**, 736 (1967).
- [12] D. Rout, S. R. Mudi, M. Hoffmann, S. Spachmann, R. Klingeler, and S. Singh, *Structural and physical properties of trilayer nickelates R<sub>4</sub>Ni<sub>3</sub>O<sub>10</sub> (R = La, Pr, and Nd)*, *Phys. Rev. B* **102**, 195144 (2020).
- [13] Z. Zhang and M. Greenblatt, *Synthesis, structure, and properties of Ln<sub>4</sub>Ni<sub>3</sub>O<sub>10-δ</sub> (Ln = La, Pr, and Nd)*, *J. Solid State Chem.* **117**, 236 (1995).
- [14] J. Zhang, D. Phelan, A. S. Botana, Y. S. Chen, H. Zheng, M. Krogstad, S. G. Wang, Y. Qiu, J. A. Rodriguez-Rivera, R. Osborn, S. Rosenkranz, M. R. Norman, and J. F. Mitchell, *Intertwined density waves in a metallic nickelate*, *Nat. Commun.* **11**, 6003 (2020).
- [15] Y.-L. Wang and B. R. Cooper, *Collective excitations and magnetic ordering in materials with singlet crystal-field ground state*, *Phys. Rev.* **172**, 539 (1968).
- [16] K. Andres, E. Bucher, J. P. Maita, and A. S. Cooper, *Observation of cooperative nuclear magnetic order in PrCu<sub>2</sub> below 54 mK*, *Phys. Rev. Lett.* **28**, 1652 (1972).
- [17] V. K. Anand, D. T. Adroja, A. D. Hillier, J. Taylor, and G. André, *Signatures of spin-glass behavior in the induced magnetic moment system PrRuSi<sub>3</sub>*, *Phys. Rev. B* **84**, 064440 (2011).
- [18] H. Yamauchi, N. Metoki, R. Watanuki, K. Suzuki, H. Fukazawa, S. Chi, and J. A. Fernandez-Baca, *Magnetic structure and quadrupolar order parameter driven by geometrical frustration effect in NdB<sub>4</sub>*, *J. Phys. Soc. Jpn.* **86**, 044705 (2017).
- [19] E. S. Clementyev, P. A. Alekseev, P. Allenspach, and V. N. Lazukov, *Soft-mode-driven magnetic ordering in the singlet ground-state system PrNi*, *Appl. Phys. A* **74**, s589 (2002).
- [20] S. Rosenkranz, M. Medarde, F. Fauth, J. Mesot, M. Zolliker, A. Furrer, U. Staub, P. Lacorre, R. Osborn, R. S. Eccleston, and V. Trounov, *Crystalline electric field of the rare-earth nickelates RNiO<sub>3</sub> (R = Pr, Nd, Sm, Eu, and Pr<sub>1-x</sub>La<sub>x</sub>, 0 < x > 0.7) determined by inelastic neutron scattering*, *Phys. Rev. B* **60**, 14857 (1999).
- [21] J. M. Tranquada, Y. Kong, J. E. Lorenzo, D. J. Buttrey, D. E. Rice, and V. Sachan, *Oxygen intercalation, stage ordering, and phase separation in La<sub>2</sub>NiO<sub>4+δ</sub> with 0.05 ≤ δ ≤ 0.11*, *Phys. Rev. B* **50**, 6340 (1994).
- [22] B. J. Campbell, S. Rosenkranz, H. J. Kang, H. T. Stokes, P. J. Chupas, S. Komiya, Y. Ando, S. Li, and P. Dai, *Long-range two-dimensional superstructure in the superconducting*

- electron-doped cuprate*  $\text{Pr}_{0.88}\text{LaCe}_{0.12}\text{CuO}_4$ , *Phys. Rev. B* **92**, 014118 (2015).
- [23] W. Koshibae, Y. Ohta, and S. Maekawa, *Theory of Dzyaloshinski-Moriya antiferromagnetism in distorted  $\text{CuO}_2$  and  $\text{NiO}_2$  planes*, *Phys. Rev. B* **50**, 3767 (1994).
- [24] W. Tabis, Y. Li, M. Le Tacon, L. Braicovich, A. Kreyssig, M. Minola, G. Dellea, E. Weschke, M. J. Veit, M. Ramazanoglu, A. I. Goldman, T. Schmitt, G. Ghiringhelli, N. Barišić, M. K. Chan, C. J. Dorow, G. Yu, X. Zhao, B. Keimer, and M. Greven, *Charge order and its connection with Fermi-liquid charge transport in a pristine high- $T_c$  cuprate*, *Nat. Commun.* **5**, 5875 (2014).
- [25] R. Comin and A. Damascelli, *Resonant x-ray scattering studies of charge order in cuprates*, *Annu. Rev. Condens. Matter Phys.* **7**, 369 (2016).
- [26] J. W. Lynn, *Two-dimensional behavior of the rare earth ordering in oxide superconductors*, *J. Alloys Compd.* **181**, 419 (1992).
- [27] H. Zhang, J. W. Lynn, W.-H. Li, T. W. Clinton, and D. E. Morris, *Two- and three-dimensional magnetic order of the rare-earth ions in  $\text{RBa}_2\text{Cu}_4\text{O}_8$* , *Phys. Rev. B* **41**, 11229 (1990).
- [28] A. Ruiz, B. Gunn, Y. Lu, K. Sasmal, C. M. Moir, R. Basak, H. Huang, J. S. Lee, F. Rodolakis, T. J. Boyle, M. Walker, Y. He, S. Blanco-Canosa, E. H. da Silva Neto, M. B. Maple, and A. Frano, *Stabilization of three-dimensional charge order through interplanar orbital hybridization in  $\text{Pr}_x\text{Y}_{1-x}\text{Ba}_2\text{Cu}_3\text{O}_{6+\delta}$* , *Nat. Commun.* **13**, 6197 (2022).
- [29] R. M. Fernandes, P. P. Orth, and J. Schmalian, *Intertwined vestigial order in quantum materials: Nematicity and beyond*, *Annu. Rev. Condens. Matter Phys.* **10**, 133 (2019).
- [30] F. Giustino, J. H. Lee, F. Trier, M. Bibes, S. M. Winter, R. Valentí, Y. W. Son, L. Taillefer, C. Heil, A. I. Figueroa, B. Plaçais, Q. S. Wu, O. V. Yazyev, E. P. A. M. Bakkers, J. Nygård, P. Forn-Díaz, S. de Franceschi, J. W. McIver, L. E. F. Foa Torres, T. Low *et al.*, *The 2021 quantum materials roadmap*, *J. Phys. Mater.* **3**, 042006 (2020).
- [31] E. Fradkin, S. A. Kivelson, and J. M. Tranquada, *Colloquium: Theory of intertwined orders in high temperature superconductors*, *Rev. Mod. Phys.* **87**, 457 (2015).
- [32] S. Wandel, F. Boschini, E. H. Da, S. Neto, L. Shen, M. X. Na, S. Zohar, Y. Wang, S. B. Welch, M. H. Seaberg, J. D. Koralek, G. L. Dakovski, W. Hettel, M.-F. Lin, S. P. Moeller, W. F. Schlotter, A. H. Reid, M. P. Miniti, T. Boyle, F. He *et al.*, *Enhanced charge density wave coherence in a light-quenched, high-temperature superconductor*, *Science* **376**, 860 (2022).
- [33] S. Lee, E. W. Huang, T. A. Johnson, X. Guo, A. A. Husain, M. Mitrano, K. Lu, A. V. Zakrzewski, G. A. De La Peña, Y. Peng, H. Huang, S.-J. Lee, H. Jang, J.-S. Lee, Y. Il Joe, W. B. Doriese, P. Szypryt, D. S. Swetz, S. Chi, A. A. Aczel *et al.*, *Generic character of charge and spin density waves in superconducting cuprates*, *Proc. Natl. Acad. Sci. U.S.A.* **119**, e2119429119 (2022).
- [34] H. Isobe, N. F. Q. Yuan, and L. Fu, *Unconventional superconductivity and density waves in twisted bilayer graphene*, *Phys. Rev. X* **8**, 041041 (2018).
- [35] A. C. Qu, P. Nigge, S. Link, G. Levy, M. Michiardi, P. L. Spandar, T. Matthé, M. Schneider, S. Zhdanovich, U. Starke, C. Gutiérrez, and A. Damascelli, *Ubiquitous defect-induced density wave instability in monolayer graphene*, *Sci. Adv.* **8**, eabm5180 (2022).
- [36] J. Nyéki, A. Phillis, A. Ho, D. Lee, P. Coleman, J. Parpia, B. Cowan, and J. Saunders, *Intertwined superfluid and density wave order in two-dimensional  $^4\text{He}$* , *Nat. Phys.* **13**, 455 (2017).
- [37] P. S. Yapa, R. Boyack, and J. Maciejko, *Triangular pair density wave in confined superfluid  $^3\text{He}$* , *Phys. Rev. Lett.* **128**, 015301 (2022).
- [38] J. A. Rodriguez, D. M. Adler, P. C. Brand, C. Broholm, J. C. Cook, C. Brocker, R. Hammond, Z. Huang, P. Hundertmark, J. W. Lynn, N. C. Maliszewskyj, J. Moyer, J. Orndorff, D. Pierce, T. D. Pike, G. Scharfstein, S. A. Smee, and R. Vilaseca, *MACS—a new high intensity cold neutron spectrometer at NIST*, *Meas. Sci. Technol.* **19**, 034023 (2008).
- [39] F. Ye, Y. Liu, R. Whitfield, R. Osborn, and S. Rosenkranz, *Implementation of cross correlation for energy discrimination on the time-of-flight spectrometer CORELLI*, *J. Appl. Crystallogr.* **51**, 315 (2018).
- [40] O. Arnold, J. C. Bilheux, J. M. Borreguero, A. Buts, S. I. Campbell, L. Chapon, M. Doucet, N. Draper, R. Ferraz Leal, M. A. Gigg, V. E. Lynch, A. Markvardsen, D. J. Mikkelsen, R. L. Mikkelsen, R. Miller, K. Palmén, P. Parker, G. Passos, T. G. Perring, P. F. Peterson *et al.*, *Mantid—data analysis and visualization package for neutron scattering and  $\mu\text{SR}$  experiments*, *Nucl. Instrum. Methods Phys. Res.* **764**, 156 (2014).
- [41] A. M. Samarakoon, K. Barros, Y. W. Li, M. Eisenbach, Q. Zhang, F. Ye, V. Sharma, Z. L. Dun, H. Zhou, S. A. Grigera, C. D. Batista, and D. A. Tennant, *Machine-learning-assisted insight into spin ice  $\text{Dy}_2\text{Ti}_2\text{O}_7$* , *Nat. Commun.* **11**, 892 (2020).